Structures 62 (2024) 106156

Contents lists available at ScienceDirect

Structures

journal homepage: www.elsevier.com/locate/structures

Computational design of segmented concrete shells made of post-tensioned precast flat tiles

Francesco Laccone [a,*], Sandro Menicagli [b], Paolo Cignoni [a], Luigi Malomo [a]

[a] Institute of Information Science and Technologies "A. Faedo" (ISTI), National Research Council of Italy (CNR), via G. Moruzzi 1, Pisa, 56124, Italy
[b] University of Pisa (Italy), Lungarno Pacinotti 43, Pisa, 56126, Italy

ARTICLE INFO

Keywords:
Concrete
Free-form surfaces
Computational design
Optimization
Digital fabrication
Finite element analysis
Mesh
Structural design

ABSTRACT

This paper introduces a novel structural concept for free-form shells, in which the shape is decomposed into flat concrete tiles to be assembled sequentially with the help of falseworks. All tiles can be prefabricated in the shop with an adaptable and reusable molding system. Once the assembly is completed, the tiles are post-tensioned through a network of cables to minimize tension and avoid detachment. The top surface can finally be completed with an in situ cast layer that fills the gaps and activates the entire shell behavior. In contrast, the bottom surface maintains a jagged aesthetics. The paper presents the automatic pipeline supporting the computational design of these shells, from an input shape to its fabrication. The segmentation of the input shape is guided by a field-aligned quad mesh derived from the principal stresses of the thin shell. The tiles are flattened individually and extruded along the normal of the best-fitting plane. In this configuration, only edge midpoints of adjacent tiles share a contact point. Thus, forces can mainly flow along the tiles' cross directions. The best configuration of cable paths and pre-loads is found by solving a constrained optimization problem exploiting a reduced model of the shell as a network of beams. Six different input shapes are tested to demonstrate the applicability of the proposed design method. The working hypotheses are validated through a higher-resolution nonlinear Finite Element Analysis. The fabrication pipeline is assessed utilizing a reduced-scale 3D-printed replica.

1. Introduction

1.1. Context

Freeform concrete shells have recently regained popularity thanks to computational tools, which allow the designer to manipulate and explore complex shapes interactively. Novel digital fabrication techniques have also narrowed the gap between digital shape and fabricated structure [1,2]. However, the actual fabrication of concrete shells, even on a small scale, still poses challenges of feasibility and cost.

In this paper, the advantages of segmentation for prefabrication in the shop are combined with the continuity provided by a final on-site casting as in Fig. 1. This approach was adopted in bold structural architectures from the past, such as the ribbed shell of Palazzetto dello Sport in Rome by Nervi. In the Nervi building system, curved precast ferrocement panels supported by falsework are eventually finished with in situ concrete. Flat prismatic tiles are the best manufacturing option because they can be produced off-site with a master mold, which can be reused several times. This strategy can achieve high efficiency, precision, and economy. Moreover, the spreading of digital fabrication has made design variations for mass customization possible and cheap. However, freeform shapes cannot be naturally split into flat tiles [3], and any discretization introduces weak lines that may alter the load path [4]. Therefore, the proposed method is based on the decomposition of free-form shells into prismatic tiles, which are aligned to the principal stress directions for structural efficiency and are flat for easy fabrication. These tiles are in contact along edge midpoints and are post-tensioned to favor a compression-only behavior. An automatic pipeline that starts from a generic freeform shape and delivers tile designs to the factory is developed. The set of cables and their pre-load are optimized, and all aspects of design and fabrication are addressed. Eventually, the shell will be completed with on-site casting.

1.2. State of the art

Fabrication of concrete shells

The success of concrete shells lies in their ability to develop membrane behavior through their shape and the possibility of the wet material being cast in any required geometry efficiently. Forming

* Corresponding author.
E-mail address: francesco.laccone@isti.cnr.it (F. Laccone).

https://doi.org/10.1016/j.istruc.2024.106156
Received 15 December 2023; Received in revised form 29 February 2024; Accepted 1 March 2024
Available online 11 March 2024
2352-0124/© 2024 Institution of Structural Engineers. Published by Elsevier Ltd. All rights reserved.

Fig. 1. Conceptual view with technical details of our concrete shell: the shape is segmented into flat tiles that are jointed at the midpoint of the edges and post-tensioned; the outer surface is finished with wire patches and in situ casting.

appropriate 3D shells requires pre-formed molds. Rigid, continuous, dense formworks have made large and accurate concrete shells feasible since ancient times, from simple barrel vaults to funicular shapes. While in the past, formworks were realized by skilled craftsmen who cut and bent wood or metal panels, nowadays additive [5] and subtractive fabrication [6] support their realization as custom single-use pieces to be assembled. However, these are labor-intensive and costly technologies, especially if the degree of reuse is limited.

The stay-in-place formwork is a new concept contributing to the gradual decrease of dense formwork. Both the mold and the surface finishing of the completed shell are formed by the same building apparatus on which concrete is cast or sprayed on site. The resulting structure is monolithic, with few or no joints. Emerging techniques involve knitted textiles [7], wire mesh [8], grid shells [9], cable nets [10], bricks or other flexible/solid patches.

Alternatively, advances in manufacturing and analysis have provided new concepts based on segmentation into panels or tiles, which may be flat, single or double-curved. The molds for these tiles are fabricable with numerically controlled machines out of different materials. However, a single mold produces a unique element, leading to a low prefabrication rate, especially in the case of variable curvature and unavoidable waste production. Flexible formworks are introduced as a viable alternative process to adapt their shape and form a variety of molds [11]. Segmented shells made of precast parts need to be assembled on-site with the inherent formation of joints, which have to be stiff and resistant to avoid hindering the shell behavior.

Reusing concrete panels from demolition is gaining popularity, pushed by a critical assessment of the entire building sector concerning the sustainability of materials and processes. The work [12] presents a 10-m arch bridge made of reused cut-out blocks. This segmented system relies on post-tensioned cables lying into drilled holes. The seams between the blocks are filled with mortar.

Design and optimization of continuous and discrete shells

The shell efficiency is inherently linked to its shape [13]. Form-finding produces effective shells showing only in-plane internal forces for specific loading and boundary conditions. Numerical form-finding techniques are available [14], such as the Force Density, the Dynamic Relaxation, and the Thrust Network Method. Numerous other derivations from these core methods support the navigation of such design space, i.e. [15,16]. However, an optimal shape is often only a first step in shell design. More structural and buildability objectives could be included in this process through dedicated optimization methods to make it feasible in the real world [17–20].

Adopting a segmented shell is practical from a manufacturing perspective, but the number of variables and aspects to handle in the design phase increases. Existing methods are specific for a given material and construction technology. A typical example is the piecewise wooden shell, which is made of plates or cassettes [21,22] combining the prefabrication potential of timber modules and their simple on-site joining. A reference example is the Armadillo Vault [23], a free-form compression-only vault made of unique polygonal stone tiles. The present work draws inspiration from the tessellation following the force lines and the extrados geometry forming disconnected planar faces. The ribbed concrete shell used as a building floor in [24] is also a relevant demountable prefabricated system. The shape is segmented into curved patches based on the stress flow, and half-joints acting as shear keys are adopted for edge-to-edge contacts. The work in [25] makes a controlled use of gaps between tiles, forming a free-form shell out of flat pieces. Their shape is optimized to have a few reusable template elements. Similarly, gaps and misalignment between flat tiles will be a prerequisite for the present paper, even though the interface of tiles is enriched with a connector and not just relying on friction as for the method in [25].

Overall, the assembly of segmented shells remains the most intricate problem [26,27] if the aim is material saving, i.e. avoiding a diffuse scaffold, which was typically used in the past for masonry vaults and arches. The authors in [28] propose a staged block insertion through suspension cables that minimized the cost and guaranteed equilibrium of the assembled shell portion. Robotic assembly can also provide the necessary restraints for bricks forming shells with specific patterns [29]. In general, finding the most appropriate assembly sequence is complex and depends on the number of blocks, the tessellation, and the target shape. The difficulties also arise with the involvement of equilibrium and deformation computation at each construction state and the possibility to adopt temporal supports as in [30]. A separate study will be dedicated to this problem.

1.3. Objectives and overview

The global objective of this research is to provide a new type of post-tensioned segmented concrete shells, fabricable in the shop out of precast tiles, along with a tailored computational method allowing their automatic design from a generic input shape. This structural system aims at providing a formwork-free alternative to materialize free-form concrete shells. This paper focuses primarily on the design methodology. Section 2 describes the genesis of the tiles from

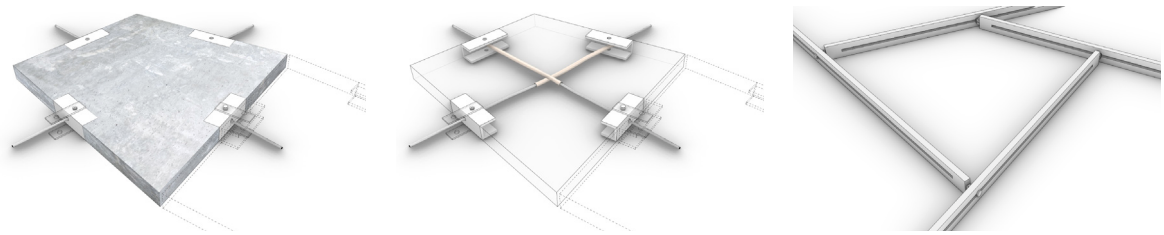

Fig. 2. (a-b) Detailed design of the prismatic tile with embedded cables' ducts and steel C-profile segments at the contact interfaces. (c) Adaptable molding system.

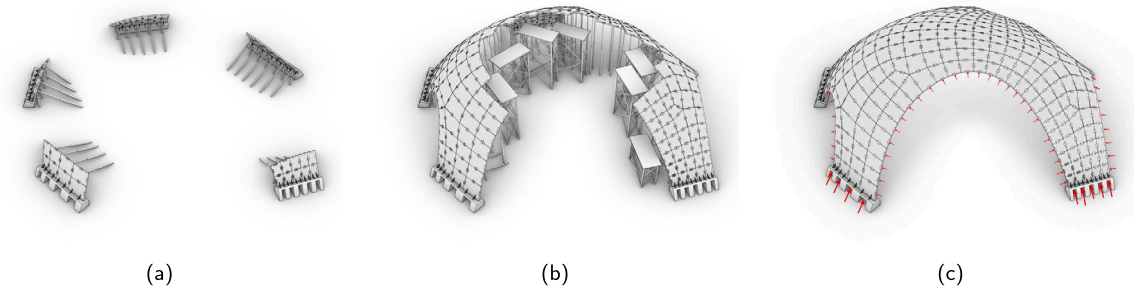

Fig. 3. Assembly: (a) laying the tiles starting from the supports; (b) sequential assembly with falseworks; (c) completion and post-tensioning.

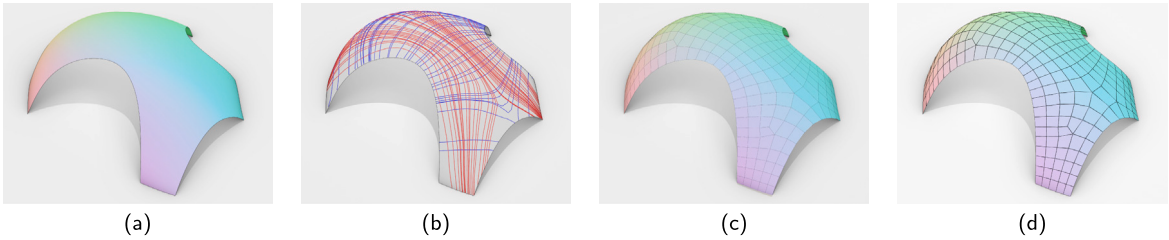

Fig. 4. Pipeline: (a) input shape; (b) stress isolines from the continuum thin shell; (c) field-driven quad mesh; (d) disjointed flat tiles.

a geometric perspective as the result of a pipeline starting from an input design shape. Other components, such as the cables and the wire mesh, are additionally defined. Section 3 includes the definition of a reduced model to size the structural members and to find an appropriate post-tensioning cable set. As a final verification step, a finite element model is built to assess the obtained results and check their accuracy (Section 4). These three steps are visualized with the support of a reference case study Igloo, shown in Fig. 1. This shell has a size of 14.85×13.00×4.73 m and is shaped as a funicular surface, having large holes on the boundary and five supports (see Table 2 in Section 5 for more statistics). Its maximum span is 14.5 m. Eventually, Section 5 reports and discusses the results achieved on other case studies with diverse input shapes. The present research expands and validates the exploratory idea presented in [31].

1.4. Concept and fabrication

The proposed concept addresses the challenges that emerged from the state of the art in concrete shell fabrication by adopting segmentation and post-tensioning. The shape is decomposed into flat quadrilateral tiles to form right prisms (with sides and faces forming 90° angles), touching each other at the midpoint of their edges. This segmented shell is efficient as long as all tiles remain in contact, i.e. the shell is compressed. Once assembled, the tiles are post-tensioned to minimize the resulting tension on the structure under service load. The outer surface is eventually completed with an in situ cast that fills the gaps and activates the shell behavior. On this basis, the shell will also develop a considerable bending strength at completion.

The shape decomposition is driven by mechanical and aesthetic purposes. Firstly, an efficient flow of forces is to be guaranteed. Second, the misalignment and gaps between the tiles are required to be as small as possible to form a pleasant, jagged appearance while avoiding concrete draining in the final in situ cast.

In this segmented assembly of tiles, by design, the adjacent faces of neighboring tiles come almost in touch at their mid side. The force transfer from tile to tile is a delicate task requiring also bending and shear capacity and is performed by a steel connector. C-profile steel segments are incorporated during the tile fabrication to avoid possible local failure due to contacts and localized loads (Fig. 2a). These steel components serve two additional functions: (a) restraining the ducts during the tiles' fabrication and (b) accommodating the connectors (bolts and plates, in dashed lines in Fig. 2b), which provide support during the assembly of the shell and stiffening for the assembled structure, since this kind of shells are not inherently rigid.

All tiles are unique and identified by a label. However, they can be prefabricated in the shop with the same adaptable and reusable molding system. One low-tech proposal for this molding system is shown in Fig. 2c. The mold walls form a reciprocal system in which the head of each beam (wall) can slide with a pin into its reciprocal. Thus, any angle and edge length can be obtained. Also, singular tiles, like triangles and polygons, can be formed with this system by adding or removing walls. Before casting, the desired mold shape is locked, and the pin channels are sealed, for instance with a PE foil running along the mold wall.

The shell assembly (Fig. 3) requires falseworks to fulfill the stability of the tiles once they are sequentially moved to their target position.

The shape curvature and the anchoring of connectors between the tiles gradually favor the formation of increasingly stable patches. The tiles are joined only through the connectors, which can transfer tension and compression as soon as the assembly is completed. So, localized bending stress could affect a tile during the assembly. Once all tiles are placed, the cables can be pushed into the ducts and post-tensioned from one extremity, applying the desired pre-load (Fig. 3c). For practical and easy access to jacks or turnbuckles at their extremities, the cables always terminate on the boundary of the shell. Once the cables have been post-tensioned, the ducts can be grouted so that the cables can be effectively coupled with concrete.

2. Geometric design

The pipeline to produce the tiles is depicted in Fig. 4. The target shape is required to be a membrane or quasi-membrane in order to keep the shell efficient and its thickness low, working primarily under in-plane loads. The input shape (Fig. 4a) is converted into a thin shell, on which a static analysis is computed under a uniformly distributed load. The resulting principal stress lines (Fig. 4b) yield a cross-field used for producing a quad mesh (Fig. 4c) and the accompanying prismatic tiles (Fig. 4d). Aligning the shell discontinuities to the stress field is a strategy also adopted in [23,24].

The faces of the quad mesh can have arbitrary curvature as in Fig. 5. A straightforward choice to obtain face planarity would be to project its vertices on the checkerboard mesh black faces (Fig. 5). The checkerboard mesh associated with the starting quad mesh is a derivation of the Varignon theorem: a polygon (i.e., Varignon polygon) formed by the edge midpoint subdivision of a control face (quad in our case) is always planar irrespective of the starting face planarity [32]. The checkerboard mesh has 'black' planar rhomboid faces and arbitrary non-planar 'white' faces. The rhomboid vertices are exactly overlapping by construction. Instead, in this work, the planarity on each face is obtained by projecting the vertices of the starting mesh on the face best-fitting plane (bottom image in Fig. 5). The higher surface smoothness, thus provided by the flat faces assembly, is preferred over the exact match at the edge midpoints, which, anyway, results in the closest points of neighboring tiles.

By adopting this strategy, the edge midpoints of two adjacent tiles will consequently be equipped with joints. Therefore, inter-tile forces can only flow through their edges' midpoint and these joints, specifically. Since the tiles are aligned with the principal stress directions, each tile is stressed mainly along its cross directions. However, if present, shear and bending forces can still be transferred through the connector.

Practically, the tiles have a proper thickness, and the extrusion of the disjointed flat faces along their normals produces overlaps and gaps (Fig. 6), which are a function of tile's curvature and size (both edge size and thickness). While gaps are acceptable to a certain extent, tile intersections are not feasible. The basic idea of the presented method is to start by having gaps only and extruding the planar face, which would minimize the gaps. Operating with a disjointed mesh, as in the present case, means solving this complex intersection problem in a discrete setup. Treating the interference of each prism individually would require solving a complex iterative Boolean intersection that eventually would not guarantee a global gap minimization.

In our approach, we proposed a simpler solution. It is easier to compute the mesh offset for both shell sides (yellow and light blue meshes in Fig. 7), which produces, in the general case, non-parallel and non-planar faces. Then, the vertices of the faces of both offset meshes are projected on the best-fitting plane, from which it is possible to gather the maximum intersection area of the two projected quads (Fig. 7). This operation leads to the minimum projected quad in the more straightforward case, i.e., in convex or concave areas. The intersection area can have multiple vertices in the general case, as shown in the red polygon in Fig. 7. To conservatively restore the initial vertex number, vertices with incident segments closest to colinear are culled, yielding the green polygon. This straightforward approach preserves

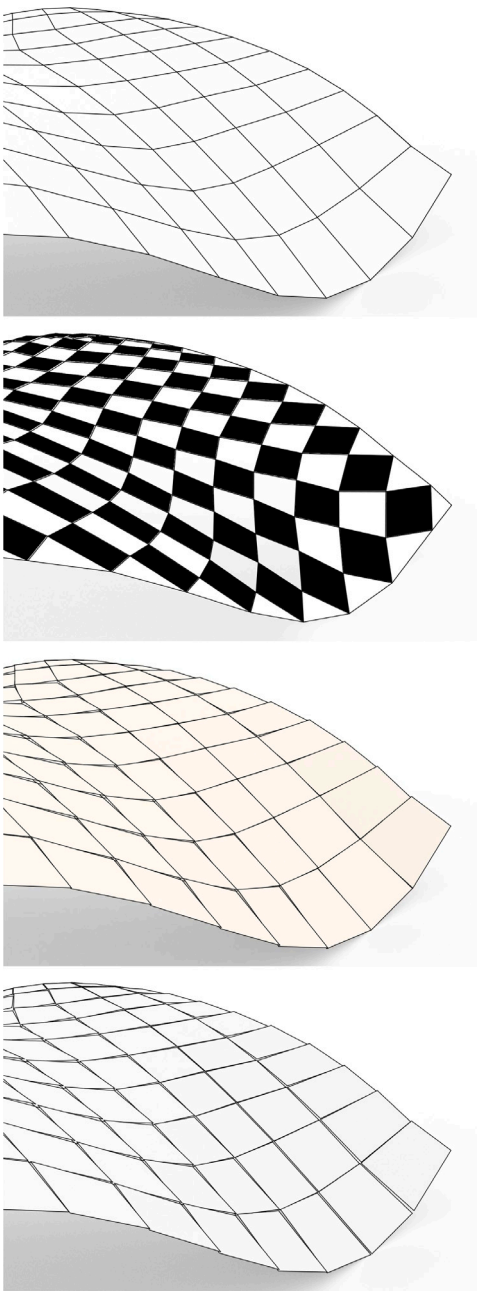

Fig. 5. From top: starting quad mesh; associated checkerboard mesh (the black faces are Varignon polygons of the starting mesh faces); flattening individual faces of the starting mesh on the checkerboard, the resulting faces share edge midpoints; flattening individual faces of the starting mesh on the best fitting plane obtaining a disjointed mesh.

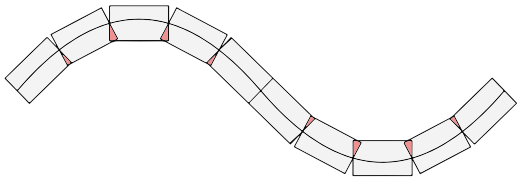

Fig. 6. The extrusion along the normal of the flat face produces overlaps and gaps among the tiles (exaggerated thickness).

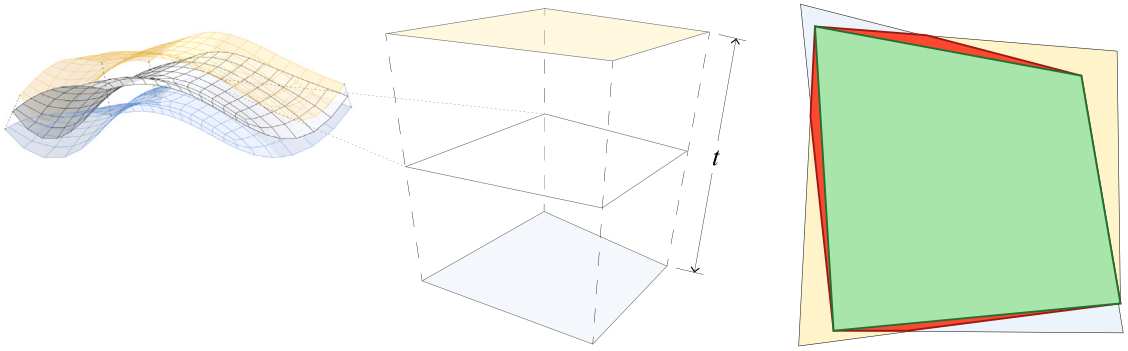

Fig. 7. Removing overlaps: the offset meshes are projected on a plane and their intersection is modified to preserve the original vertex number (the green polygon is kept while the red parts are culled). In the example the extrusion thickness t is exaggerated for visualization purposes only. (For interpretation of the references to color in this figure legend, the reader is referred to the web version of this article.)

the number of vertices per face and depends on the selected thickness of the shell: the lower the thickness, the closer the tiles. Attaining a fixed gap size is a more complex problem and would require a dedicated optimization because the curvature is variable. In the current approach, the obtained gaps are the smallest possible. However, larger gaps, which the concrete rheology may require of the final cast, can be achieved by offsetting the yellow and light blue faces inward by a desired amount.

Selecting the tiles' size requires finding a trade-off between shape fidelity and design economy. Overall, a coarser mesh leads to fewer elements to design and install. A finer mesh better approximates the target shape but turns into a larger number of tiles, connections, cables, and more intense construction works. For the Igloo case, a target edge length of 0.7 m is considered, with the aim of favoring the homogeneity of tile size. Suppose being on a section of the shell input shape, the target edge length can be regarded as a chord that, at the maximum curvature of 0.229 m^{-1}, yields an angle at the center of 4.61° and a sagitta of 0.015 m. This value is the maximum distance between the shape and the center of a mesh quad face. While the curvature lowers, the shape approximation is even better: areas with smaller curvature are smoother, and vice versa. Through the application of the Best Fitting Plane projection in the construction process, proximity between mesh face centers and edge midpoints to the target shape is ensured. Consequently, the load paths along the principal stress lines, traversing these points on flat faces, are representative of the target shape. It is important to note that while the use of plane projection may introduce a greater distance around face vertices, these areas exhibit a limited mechanical scope.

Cables lie by design on the mid-surface of the shell to globally exert compression in plane once the structure is post-tensioned. First, a large and distributed set of all possible candidate cables is computed. Then, their pre-load is found by solving an optimization problem (Section 3). Candidate cable paths are found by chaining the segments linking pairs of opposite edge midpoints for each tile (Fig. 8a). Since the quad mesh is aligned to the principal stress, the cable paths are also aligned to them by construction.

Three conditions determine the discarding of cable paths from the candidate set. The first condition discards paths that are not terminating on the boundary. It can be the case of closed loops or paths terminating on a singular point. Hence, it is practically not possible to access the cable terminals for exerting post-tensioning. The two other conditions are based on path kinks. By design, the cable path through the tiles is straight, while it has kinks at the connectors. Hence, it is diverted and curves abruptly, pre-loading the tiles. The cable curvature is a function of the angle and the gap between the tiles. The allowable maximum cable curvature poses a first limitation on the angle in 3D formed at the kinks, i.e., to avoid cable damage. The efficiency of pre-loading poses a second constraint. A kink is beneficial if it introduces a transversal compression, which is obtained if the cable kink locally lies in a plane orthogonal to the surface. Conversely, the cable also induces an undesired in-plane shear if the kink component on the surface tangent plane is relevant. Therefore, a second constraint to limit the shear applies to the angle formed by the cable segments projected on the tangent plane at each kink.

The experiments in this paper adopt a single theoretical condition $\alpha_{lim} = 150°$ for the angle in 3D. The aim is to avoid overconstraining the optimization space since the more cables are discarded, the smaller the number of available combinations of cables and pre-loads to remove tension from the tiles. The adopted value corresponds to an approximate curvature radius of 10 diameters. With reference to Fig. 8a, paths with $\alpha < \alpha_{lim}$ are removed from the set of valid cables.

To add redundancy and to fill the gaps between the tiles while providing a finishing of the structure, an in situ cast is arranged on the outer surface of the structure. This cast embeds a fiberglass or steel wire mesh. As a last step of the pipeline, wire mesh patches are designed as in Fig. 9. The method is based on clustering portions of the outer surface starting from a uniform distribution of seeds (Fig. 9a). Then, the target double-curved surface is decomposed into developable flat patches with specific shapes and cuts to be laid on the shell without significant distortions or wrinkles (Fig. 9b). To comply with fabrication constraints, the number of seeds is tuned to obtain patches that fit into the size of commercially available sheets of material (Fig. 9c). The pipeline results in a labeled set of prismatic tiles, cable segments, and wire mesh patches, which are all easily fabricable.

3. Structural design

3.1. Model reduction and sizing

The complexity of designing the components of the present structural system is due to the way they are combined and the large number of material and geometric discontinuities. Based on geometric and system features, this complexity can be reduced by adopting simplifying hypotheses. The mesh faces are aligned with the principal stress directions as in Fig. 10, so the incoming actions on each tile are primarily orthogonal to their edges. The tile shear is negligible. Additionally, the interaction of tiles is enforced only through a connector at the edge mid side, so the force transfer occurs only in that area. The connector also bridges the gaps between the tiles. The tiles show a predominant strut-and-tie behavior along the two crossing directions. Therefore, the structure can be modeled as a grid of beams, where a pair of crossing beams can replace each tile. For simplicity, the model do not have gaps, and the beams have rigid joints at the tile centers and the tile edges.

The reduced model has an additional practical use for the intent of preliminary sizing the tile. Since the tile corners are mostly inactive in this phase, the tile size and connection detail can be designed by looking only at the compressive axial forces in the crossing beams. In

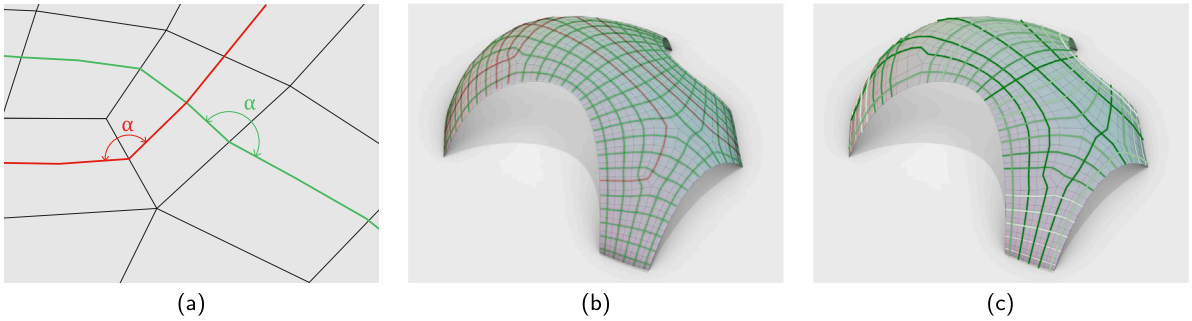

Fig. 8. Selection of cable paths: (a) closeup on candidate cable path (green) and discarded path (red); (b) all candidate and discarded paths; (c) cables after the optimization as per Eq. (1) (the darker, the higher the pre-load). (For interpretation of the references to color in this figure legend, the reader is referred to the web version of this article.)

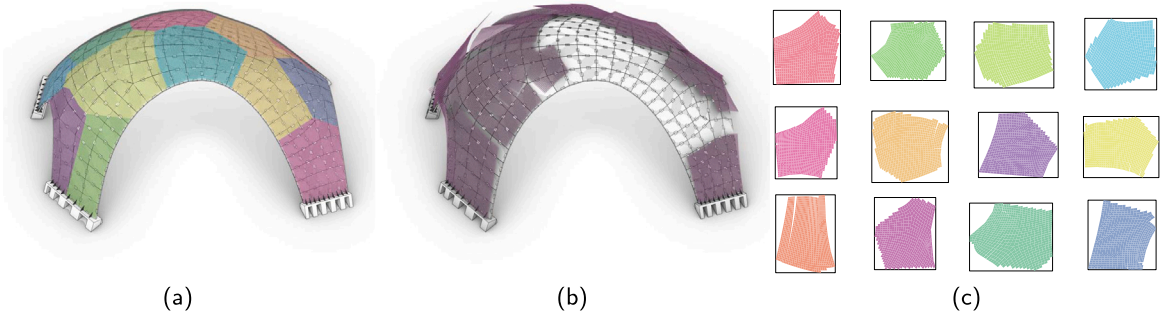

Fig. 9. Minimum distortion patches of wire mesh to lay on the top face of the shell: (a) developable patches; (b) flat sheets of material; (c) 2D flat patches.

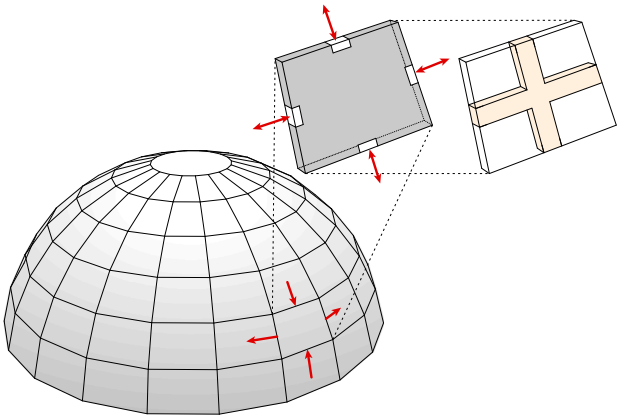

Fig. 10. Reduced model derived from the force flow. The tiles are aligned to the stress isolines, and the contact points are only at the edge mid side.

particular, the thickness and width of the beams are defined by the tile thickness and C-profile length, respectively. The size can be updated after the post-tensioning optimization (Section 3.2), when the cable pre-loads have increased the compression. All experiments of this paper adopt the same cross sections, 0.06×0.18 m (tile thickness × C-profile length), and the same C28/35 concrete as a material.

The Serviceability Limit State (SLS) loads adopted in the optimization is the sum of the structural weight and $\gamma_q q_k = 1.5 \times 0.5$ kN/m^2, where q_k is the characteristic live load and γ_q is the corresponding partial factor. Note that in this phase, the additional in situ casted layer is considered as a wet-concrete load, and its contribution in terms of stiffness is neglected to be on the safety side, as the only load-bearing system was the post-tensioned tiling. At the starting condition (with no cables), the reduced model analysis confirms the effectiveness of the meshing and the model reduction strategies. It shows a prevailing axial regime (Fig. 11a), low bending moments and shear forces (Fig. 12).

3.2. Post-tensioning optimization

The cable path is a polyline changing direction from tile to tile. The pre-load can be seen as punctual forces exerted on the shell at the kinks, which occur each time the cable path is diverted at a connector. Thus, punctual deviation forces are affixed to the steel parts of the tiles, avoiding the risk of failure due to local pressure. In this phase, post-tensioning losses are neglected, so tangential pre-load components are null, and the cable is uniformly tensioned. In the reduced model, the cable overlaps a subset of beams, and the pre-load effect is applied at the beam endpoints if a kink occurs as in Fig. 13.

Given the jth cable, its effect on the structure is modeled as a vector of equivalent loads F_j acting at the kinks. Assuming for simplicity to operate in a linear setup, the internal forces in beams produced by each F_j can be superimposed on the results of a linear analysis under service load. Furthermore, because of linearity, the cable effect can be scaled by a factor, i.e., its pre-load p_j. Similarly to [33], selecting appropriate cables and their accompanying pre-load requires the solution of a constrained minimization problem:

$$min \sum f_t(p_j) \tag{1}$$

$$s.t.\ 0 \le p_j \le p_{max} \tag{2}$$

where $\sum f_t$ is the sum among all beams of only the positive (tension) axial forces. The internal forces are pre-computed for all configurations: one for the SLS scenario and one for each cable equivalent-load scenario. In this latter case, a pre-load of 1 kN is adopted so that its effect can be linearly scaled and superimposed on the others to achieve the minimum of the objective function. The value p_j provides directly the pre-load to be assigned to each cable. The equilibrium of the structure holds as a superimposition of multiple equilibrium conditions. Eq. (2) defines a limitation on the allowable pre-stress on each cable.

The optimization problem of Eqs. (1)–(2) is solved using two algorithms from the NLopt library [34] in sequence: CRS2, for global evolutionary search, and BOBYQA, a derivative-free local refinement. For the Igloo case study, the entire cable set after filtering comprises

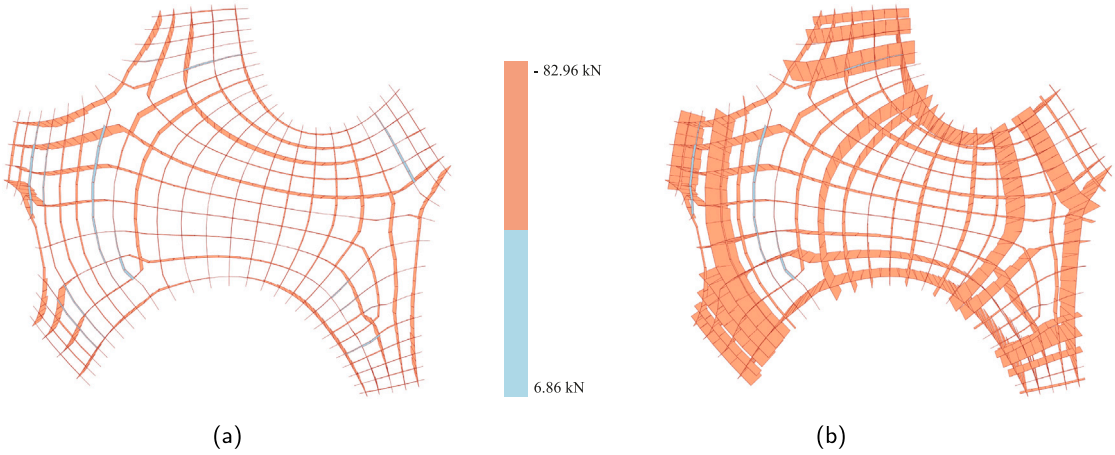

Fig. 11. Axial forces in the reduced model linear analysis: (a) starting shell under SLS loads; (b) shell deploying optimized cables.

Table 1
Parameters adopted in the FE model.

Component	FE type	Material	Density (kN/m^3)	Young's Mod. (GPa)	Poisson ratio	Exp. coeff.	Dimension (m)
Tile	S4R	Concrete	25	32	0.3	–	0.06 (thick.)
Cable	B31	Steel	78.5	210	0.3	1.20E−05	0.008 (diam.)
Connector	RB3D2	–	–	–	–	–	–

44 cables (see Fig. 8c). A 8 mm diameter cable is adopted, having an allowable pre-stress p_{max} = 50 kN. The optimization leads to a significant reduction of positive axial forces on the elements (−86.6%), as shown in Fig. 11b, and an overall improvement of the shell statics (see Table 3 for additional results). The benefits of cable pre-load in reducing also bending moments cannot be captured by the current model, as it is based only on balancing internal axial forces and not beam stress.

4. Verification

The computational design has introduced several structural modeling and analysis simplifications to find the internal forces within a low computational time. However, the lack of information concerning stress in the panels and the need for a more appropriate simulation of the actual structural elements suggest to perform a verification step.

For a precise evaluation of the structural performance, the shell should be modeled with solid parts, including the details of the connections and the force transfer from the cables. In particular, the components' interface should include adhesion between concrete and steel and nonlinear contacts between the tiles. The simulation of the completed shell should include the completion cast in a final stage, firstly as a wet-concrete load only and later as an additional structural layer adhering to the tiles. This strategy would increase the simulation costs and introduce several uncertainties that shall be solved at a later design level, eventually supported by calibration through physical testing on parts of the shell or its connection system.

The adopted strategy, instead, is more compatible with the current detail level of a preliminary design and neglects contact nonlinearities. The model relies on shell finite elements for the tiles, beams for the cables, and node constraints for the contacts of the different parts. This verification is conducted through a geometrically nonlinear model built and analyzed with the ABAQUS package [35]. The verification model is generated with an automated workflow developed in conjunction with the algorithm employed for the computational design in a Python environment.

As the outcome of the geometric design (Section 2), the disjointed mesh is remeshed as a quad element with a subdivision level 3. The mid side nodes of each tile are connected with the neighboring ones with a 3-node polyline, representing a rigid joint between the tiles. The cable segments are anchored at the central nodes of these polylines so that the post-tensioning is transmitted through the connector to the tiles. Each tile is clamped to the adjacent one through bolts and plates. To model such bending restraint, the mesh nodes belonging to a spherical neighborhood of each connector are tied to the accompanying rigid node. The rigid body transfers stress among tiles and cables but can have no stress. Fig. 14a reports the finite element model of the Igloo case. All nodes at the base of the shell have all degrees of freedom fixed. The cable endpoints that are fixed to the ground have pin joints.

The materials used in the analysis are linear elastic isotropic; their specifications are provided according to Section 3, and are reported with the accompanying finite elements in Table 1. As shown in the schematics of the connection (Fig. 14b), the interface of the tiles is the most critical point of the model. The rigid body connecting the tiles (RB3D2 finite element, green in Fig. 14b) is referenced with its midpoint (blue). The cable segments (B31 finite elements, in red) are anchored with pins. Even though the connection of the tiles through the rigid bodies would be highly conservative as it is akin to a pin joint, the shell mesh (S4R finite elements) would lack restraints and be unstable. Instead, the mesh vertices on both sides of the rigid body, as highlighted in orange in Fig. 14b, are tied to the reference node to provide a more realistic constraint. All elements are merging or interacting only around the rigid body. For instance, cables and shells share no contact. As this connection may appear over-conservative, please consider that bending stiffness also arises from the interaction of vertical faces of adjacent tiles if properly considered as 3D elements.

The analysis simulates the assembly stages of the shell and consists of two steps ramping three loads:

- a gravity load pertaining to all bodies endowed with a density as for the dead load, applied at step 1 and propagated;
- a post-tensioning load applied on the cables, applied at step 1 and propagated;
- a uniform load simulating the SLS on the tile faces, applied at step 2.

The cable post-tensioning is introduced as a custom temperature field on each cable segment based on the optimization results. Thus, a negative temperature variation induces a shrink in the segment, simulating

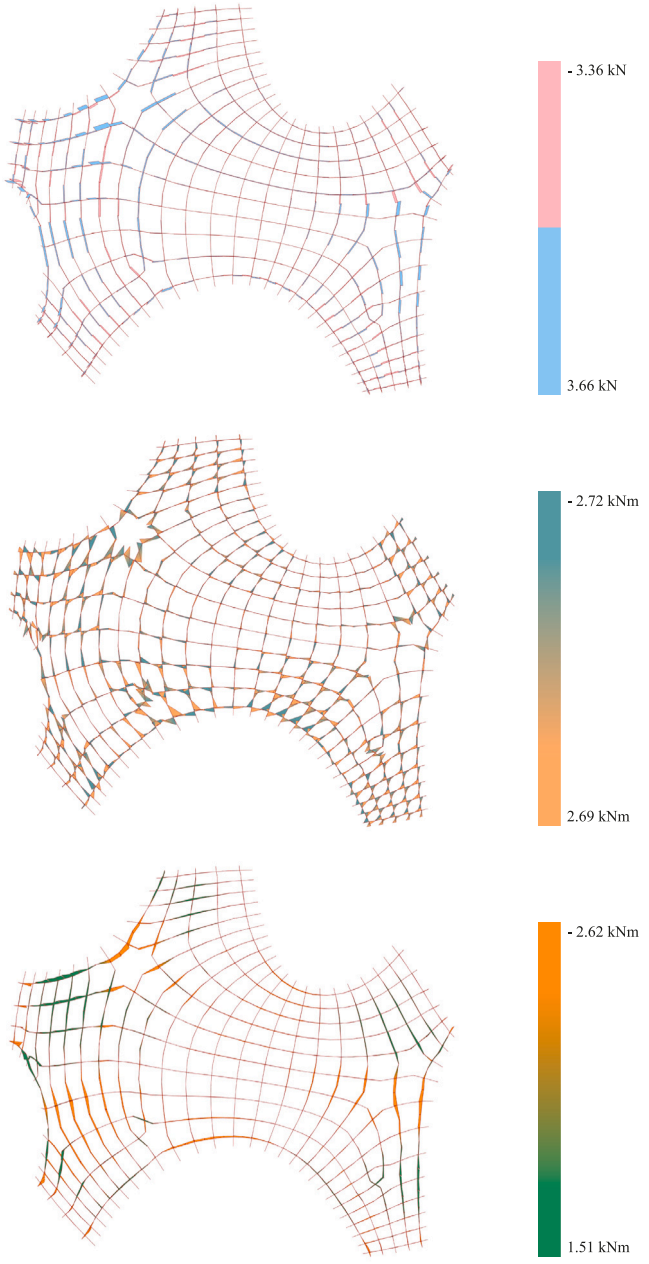

Fig. 12. Other internal forces in the reduced model linear analysis at the starting condition under SLS loads, from top: in-plane shear, in-plane and out-of-plane bending moments.

the effect of cable sliding and force transfer without pre-load losses. Likewise, an exact simulation of the real mechanics of the present structures would have required three stages: post-tensioning of cables and dead load, shell completion, and live load. The possibility of mobilizing an additional stiffness provided by the completion of in situ casting is not taken into account.

Figs. 15 and 16 report the main results of the verification analysis at the end of load step 2. Results reveal that the shell has a good stiffness under SLS loads as the higher deformation occurring on the tiles is located on the largest opening and is smaller than 4 mm (Fig. 15 top), with reference to the maximum span of 14.5 m. The other two frames of Fig. 15 show the maximum and minimum principal stress on the tiles. The most interesting feature is that the stress fields are aligned with the tiling directions, demonstrating the effectiveness of the adopted segmentation strategy. The maximum principal stress is

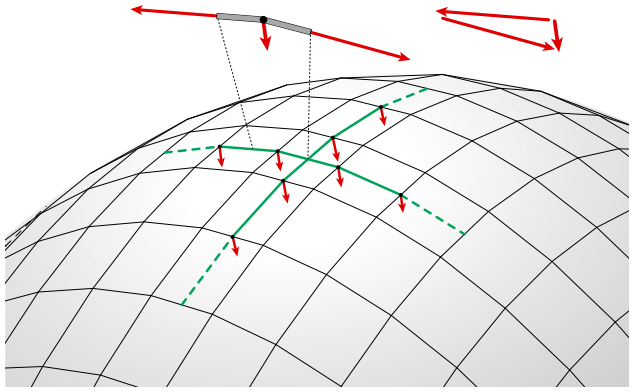

Fig. 13. Cable post-tensioning: equivalent load applied at the kinks of cable paths (in green); resulting force at a node from a uniform pre-load. (For interpretation of the references to color in this figure legend, the reader is referred to the web version of this article.)

relatively low and overall smaller than 1 MPa. The only exception is a peak in the left top support caused by the external constraint. The minimum principal stress is limited to a small range of up to −7.7 MPa. The contour map denotes the formation of a grid of load paths following the stress isolines on the ideal shell (see Fig. 4b) and the cable paths, accordingly. Ideally, the maximum utilization areas overlap the beams of the reduced model, confirming that the adopted model reduction strategy is suitable for preliminary sizing as the corners of the tiles are less utilized parts and can be neglected. The current and the reduced model are in agreement in terms of stress, being −7.68 MPa in compression 0.63 MPa in tension the values computed with the axial forces in Fig. 11.

The reduced model cannot provide information on the cables' status since they are treated as equivalent loads. Instead, the cables are explicitly included in the verification model, even if each cable segment is treated as if it is independent for simplicity. Fig. 16 displays the cable usage in terms of axial forces. All cables are active, and there is no decompression due to other loads. The maximum axial force reaches the value of about 60 kN as a joint effect of pre-load and force induced by external loading.

5. Implementation and results

Several shapes are considered to demonstrate the validity of the present concept (see Fig. 17). All of them are input to the design pipeline with the aim of proving that they can perform with a sufficient load-bearing capacity. The shapes are characterized by various sizes, geometric features, openings, and boundary conditions (Table 2). Arch and Hypar have a predominantly negative Gaussian curvature and rely on few supports. All others are funicular or quasi-funicular shapes. In particular, Neumunster, named after the famous grid shell in Luxembourg, is pillow-shaped and continuously supported along the boundary.

The geometric design pipeline is implemented in Rhino-Grasshopper environment [36], the starting mesh is derived from the Rhino quad remesher, using as guides the stress isolines, which are an output of a linear static analysis in Karamba3D [37]. The optimization also uses static analysis feedback provided by the solver Karamba3D. For the optimization, the plugin [38] implementing the NLOPT library is used. All examples implement the same design strategies and share the same parameters so that the structural system is uniform:

- the examples have various sizes and number of faces; however, they are remeshed targeting a similar average edge length of 0.70 m since, for discrete structural systems to be comparable, grid spacing and topology should be kept uniform;

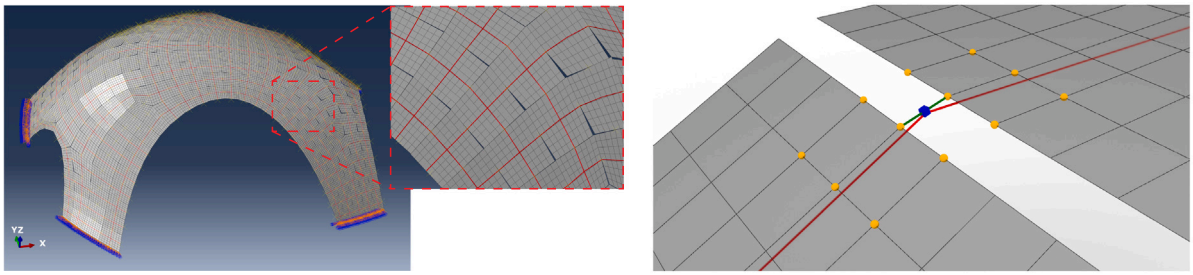

Fig. 14. Verification model: (a) assembled Abaqus model with closeup (shell elements in gray, cables in red, rigid bodies reference points are yellow crosses); (b) schematics of the connection in an exaggerated perspective view (rigid body in green with its reference point in blue, orange spheres indicate shell nodes that are tied to the reference point). (For interpretation of the references to color in this figure legend, the reader is referred to the web version of this article.)

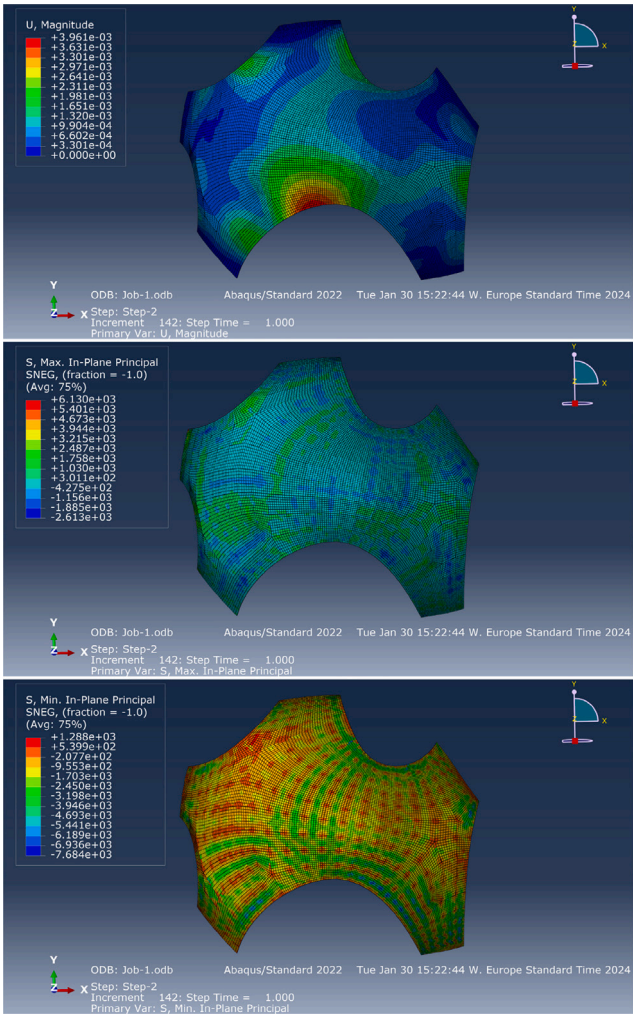

Fig. 15. Staged nonlinear analysis results from the verification model. Shell parts only at the end of load step 2, from top: displacement magnitude, maximum in-plane principal stress, minimum in-plane principal stress. Displacement units are m; stress units are kPa.

- the tiles used in all examples have constant thickness t = 0.06 m and the same connection design with the embedded steel C-profile;
- cables have 8 mm diameter and an allowable pre-stress $p_{max} = 50$ kN;
- material properties are specified in Table 1;

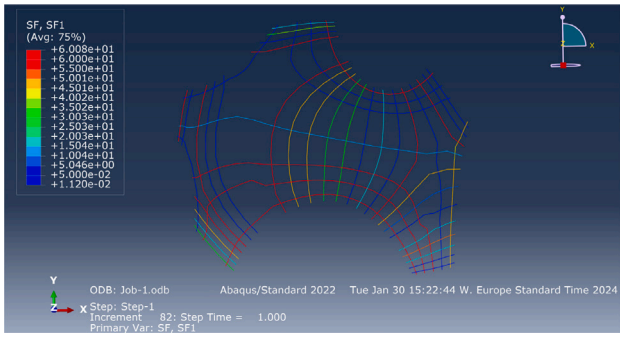

Fig. 16. Staged nonlinear analysis results from the verification model. Cables view only at the end of load step 2: axial forces. Force units kN.

- the structural elements of the reduced model are sized as in Section 3, the dead load is computed from the material density and geometry of the cross sections, while the SLS loads (including the remaining dead) is applied as a lumped load on each tile center;
- each cable is initialized with a pre-load of 1 kN, the pre-loads are updated by solving the optimization problem in Eqs. (1)–(2);
- material and geometric non-linearities are neglected in all cases for the reduced model analysis.

Table 3 reports the representative results for all examples. The objective function, i.e., the sum of axial tension force, is significantly reduced (up to a complete removal) after deploying cables with optimized tension. In all cases, the stiffness of the structure is improved or at least preserved, as suggested by the maximum displacement. The cables cause an increase of compression forces from +3% for the Arch to +135% for the Igloo. However, the maximum stress among all cases is 9.45 MPa for the Hypar and results well within the concrete strength limit. The pre-compression induced by the cable post-tensioning improves the reliability of the system as the decompression risk and formation of cracks are mitigated, and the material is more efficiently used. Regardless, tension forces that cannot be canceled are still very low (less than 1 MPa in the Sail case).

Overall, the structural improvement strongly depends on the shape geometry and its statics-driven tessellation. Indeed, irregularities on the mesh, such as mesh singularities and local distortions of the grid, introduce discontinuities in the flow of forces. Moreover, these points are usually not crossed by cables because of the filtering in Section 2, reducing the chances of local tension forces being caught by a cable. For instance, the Arch example has regular geometry and mesh, two cables crossing all its tiles, and the space of variables is quite ample so that a solution with a null objective function can be more likely found. Conversely, the Neumunster example has quite an irregular mesh, although it has the best possible shape and boundary condition.

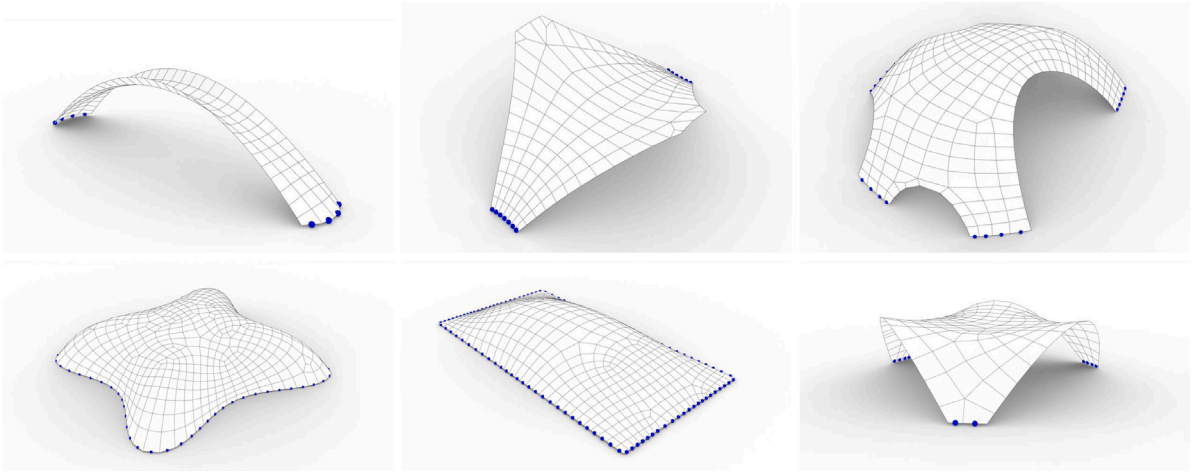

Fig. 17. Experimental dataset of surfaces, from top left: Arch, Hypar, Igloo, Lilium, Neumunster, Sail. All models are tessellated with the actual quad mesh used to derive the tiles; blue spheres indicate fixed supports.

Table 2
Dataset statistics (with reference to Fig. 17): Case name, axis-aligned bounding box size, number of faces of the mesh equaling the number of tiles, number of connection details (including either connection between tiles and on the open boundary), average edge length of the tiles, surface area and number of valid cables used in the optimization.

Case name	Size (mxmxm)	Num. faces $\|F\|$	Num. conn $\|C\|$	Avg. edge length $\tilde{l}$ (m)	Surface S (m^2)	Num. cables j
Arch	3.24 × 20.95 × 4.85	128	292	0.73	69.12	36
Hypar	8.78 × 11.75 × 4.32	158	341	0.67	70.70	29
Igloo	14.85 × 13.00 × 4.73	269	574	0.74	150.85	44
Lilium	17.96 × 19.67 × 5.00	639	1293	0.81	398.78	23
Neumunster	10.00 × 20.00 × 2.50	483	1006	0.66	219.98	46
Sail	11.33 × 11.00 × 3.19	170	348	0.78	102.31	18

Table 3
Analysis results from the reduced model under SLS loads (Start condition) and after the post-tensioning optimization (Optimized). The table reports the maximum Euclidean displacement δ_{max}, the ratio of the maximum displacement to the maximum span S, the maximum axial compression and tension ($f_{c,max}$ and $f_{t,max}$, respectively), the sum of tension forces $\sum f_t$, and finally the tension reduction in the objective function Δ.

Case name	Start condition					Optimized					Reduction
	δ_{max} (m)	δ_{max}/S –	$f_{c,max}$ (kN)	$f_{t,max}$ (kN)	$\sum f_t$ (kN)	δ_{max} (m)	δ_{max}/S –	$f_{c,max}$ (kN)	$f_{t,max}$ (kN)	$\sum f_t$ (kN)	(%)
Arch	0.004	0.0002	49.62	2.21	12.36	0.004	0.0002	51.30	0.00	0.00	−100.00
Hypar	0.050	0.0043	77.98	36.07	481.14	0.050	0.0043	102.12	0.00	0.00	−100.00
Igloo	0.020	0.0014	35.30	8.06	582.54	0.020	0.0014	82.96	6.86	78.07	−86.60
Lilium	0.006	0.0002	30.56	6.91	224.71	0.006	0.0002	66.46	0.78	7.55	−96.64
Neumunster	0.005	0.0003	30.50	7.35	359.85	0.004	0.0002	69.34	4.47	75.90	−78.91
Sail	0.080	0.0075	59.52	10.85	426.22	0.060	0.0056	84.36	10.44	98.19	−76.96

For this example, 6 over 52 cables are filtered out, thus reducing the design space. For the proposed system, good meshing is a trade-off of smoothness and fidelity to the stress field.

A shell has been fabricated in a small-scale context as a practical feasibility proof of these structures. The fabrication pipeline is developed from the geometric design outcome and provides the labeled tiles and cables to fabricate or cut. The final aim is to assess the assembly routine on a scale model as in Fig. 18. The tiles are 3D-printed with PLA material, and for each edge midpoint, they are provided with a pin that can be used to tie the adjacent tile using a rubber band. This detail mimics the plates and bolts provided in the full-scale system and allows a cantilevering assembly procedure without scaffolding. The tile has a 3D printed label, and its alignment provides the correct positioning on the ideal surface. Labeling all tile midpoints could be a more reliable system for a large scale or a different fabrication technique. The start and end labels unambiguously define cables, as the example is relatively simple to guess all cable paths without computation. At completion, the cables are tensioned and locked with an anchor. A 3D digital model supported the assembly.

6. Conclusions

This paper presents a design method that is an alternative to traditional concrete shells in mechanics and fabrication. It is expected to be highly competitive for non-standard shapes, offering cost savings. The method is rooted in a new structural concept and exploits an automated pipeline to deliver segmented shells made of prismatic tiles, which are easily fabricable and can be handily assembled to form a proper structure. To guarantee discrete tiles to develop a suitable load-bearing scheme, the meshing adopted an alignment to the principal stress directions, and to avoid detachment, the tiles are post-tensioned utilizing optimal embedded cables.

The method works for complex shapes having various geometric features. It can handle several design variables to tune the stiffness and strength of the final solution. However, the efficiency of this system is higher in areas of double curvature where the geometry of the shape and the post-tensioning load provide the best contribution. In a preliminary assessment, the produced structures appear quite stiff

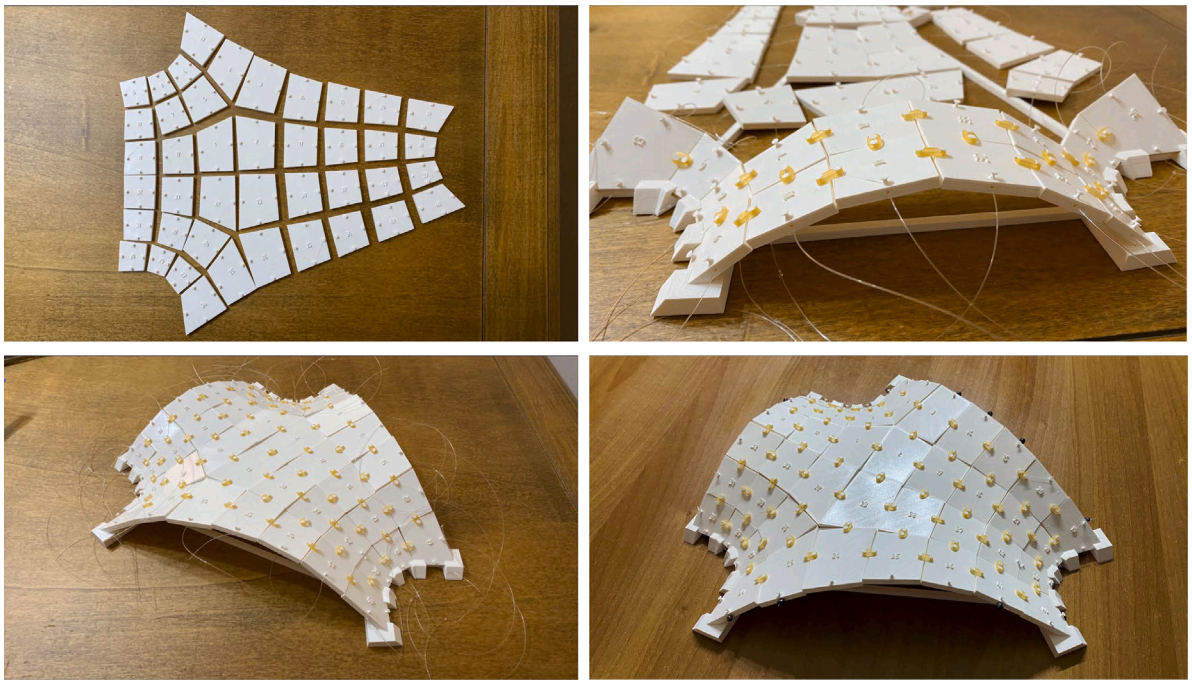

Fig. 18. Assembly steps of a 3D printed demonstrator.

and robust. The main limitation of this method is that the input shape is required to be a membrane or quasi-membrane. In the presence of flat and cantilevering parts, the bending moments can hardly be balanced by a plausible in-plane configuration of cables. Moreover, the mechanical model adopted here is not able to catch the potential reduction of bending-induced tensile stress. A fundamental step is delivering the initial quad mesh, which is required to have regular and stress-aligned tiles. Moreover, the meshing can strongly influence the chances of effectively post-tensioning the shell since it is responsible for the cables' placement.

Several topics deserve further research efforts. On the structural side, the system relies on multiple redundancy layers, such as post-tensioning, bending stiffness of the connectors, and completion cast. However, their contribution to the statics and stability is to be investigated. The structural model adopted, as a grid of beams in accordance with the meshing and load transfer mechanism, could represent a lower-bound solution. The structural response has been evaluated with more advanced simulation. However, it is still not sufficient to understand all aspects affecting the structural behavior. Solid simulation is recommended, considering the tiles' contacts and a real-scale testing campaign.

On the practical side, the essential topic is investigating fabrication tolerances and the effect of the size of the gaps between the tiles. Production and physical experiments could provide relevant insight to improve the design method. The assembly is also an open problem. The assembly of the small-scale prototype has revealed a potential for building some portions of the shell in a self-supporting fashion. This attitude is a function of the geometry and the statics and can provide room for future investigation.

Declaration of competing interest

The authors declare that they have no known competing financial interests or personal relationships that could have appeared to influence the work reported in this paper.

References

[1] Li W, Lin X, Bao DW, Xie YM. A review of formwork systems for modern concrete construction. Structures 2022;38:52–63.

[2] Wangler T, Lloret E, Reiter L, Hack N, Gramazio F, Kohler M, et al. Digital concrete: opportunities and challenges. RILEM Techn Lett 2016;1:67–75.

[3] Jiang C, Wang C, Tellier X, Wallner J, Pottmann H. Planar panels and planar supporting beams in architectural structures. ACM Trans Graph 2022.

[4] Oval R, Rippmann M, Mesnil R, Van Mele T, Baverel O, Block P. Feature-based topology finding of patterns for shell structures. Autom Constr 2019;103:185–201.

[5] Naboni R, Breseghello L. High-resolution additive formwork for building-scale concrete panels. In: Bos FP, Lucas SS, Wolfs RJ, Salet TA, editors. Second RILEM international conference on concrete and digital fabrication. Cham: Springer International Publishing; 2020, p. 936–45. http://dx.doi.org/10.1007/978-3-030-49916-7_91.

[6] Martins PF, de Campos PF, Nunes S, Sousa JP. The tectonics of digitally fabricated concrete. a case for robotic hot wire cutting. In: Wangler T, Flatt RJ, editors. First RILEM international conference on concrete and digital fabrication – digital concrete 2018. Cham: Springer International Publishing; 2019, p. 311–22. http://dx.doi.org/10.1007/978-3-319-99519-9_29.

[7] Popescu M, Rippmann M, Liew A, Reiter L, Flatt RJ, Van Mele T, et al. Structural design, digital fabrication and construction of the cable-net and knitted formwork of the KnitCandela concrete shell. Structures 2021;31:1287–99.

[8] Dörfler K, Hack N, Sandy T, Giftthaler M, Lussi M, Walzer AN, et al. Mobile robotic fabrication beyond factory conditions: Case study Mesh Mould wall of the DFAB HOUSE. Constr Robot. 2019;3:53–67.

[9] Tang G, Pedreschi R. Gridshell as formwork: Proof of concept for a new technique for constructing thin concrete shells supported by gridshell as formwork. J Archit Eng 2020;26(4):04020036.

[10] Méndez Echenagucia T, Pigram D, Liew A, Van Mele T, Block P. A cable-net and fabric formwork system for the construction of concrete shells: Design, fabrication and construction of a full scale prototype. Structures 2019;18:72–82, Advanced Manufacturing and Materials for Innovative Structural Design.

[11] Hawkins WJ, Herrmann M, Ibell TJ, Kromoser B, Michaelski A, Orr JJ, et al. Flexible formwork technologies – a state of the art review. Struct Concr 2016;17(6):911–35.

[12] Devenes J, Brütting J, Küpfer C, Bastien-Masse M, Fivet C. Re: Crete–Reuse of concrete blocks from cast-in-place building to arch footbridge. Structures 2022;43:1854–67.

[13] Adriaenssens S, Block P, Veenendaal D, Williams C. Shell structures for architecture: form finding and optimization. Routledge; 2014.

[14] Veenendaal D, Block P. An overview and comparison of structural form finding methods for general networks. Int J Solids Struct 2012;49(26):3741–53.

[15] Millar C, Mitchell T, Mazurek A, Chhabra A, Beghini A, Clelland JN, et al. On designing plane-faced funicular gridshells. Int J Space Struct 2021;09560599221126656.

[16] Miki M, Adiels E, Baker W, Mitchell T, Sehlström A, Williams CJ. Form-finding of shells containing both tension and compression using the airy stress function. Int J Space Struct 2022;37(4):261–82.
[17] Bletzinger K-U, Ramm E. Structural optimization and form finding of light weight structures. Comput Struct 2001;79(22–25):2053–62.
[18] Gabriele S, Varano V, Tomasello G, Alfonsi D. R-Funicularity of form found shell structures. Eng Struct 2018;157:157–69.
[19] Gil-Ureta F, Pietroni N, Zorin D. Reinforcement of General Shell Structures. ACM Trans Graph 2020;39(5).
[20] Meng X, Xiong Y, Xie YM, Sun Y, Zhao Z-L. Shape–thickness–topology coupled optimization of free-form shells. Autom Constr 2022;142:104476.
[21] Robeller C, Von Haaren N. Recycleshell: wood-only shell structures made from cross-laminated timber (CLT) production waste. J Int Assoc Shell Spatial Struct 2020;61(2):125–39.
[22] Bechert S, Sonntag D, Aldinger L, Knippers J. Integrative structural design and engineering methods for segmented timber shells - BUGA Wood Pavilion. Structures 2021;34:4814–33.
[23] Rippmann M, Van Mele T, Popescu M, Augustynowicz E, Méndez Echenagucia T, Calvo Barentin C, et al. The Armadillo Vault: Computational design and digital fabrication of a freeform stone shell. In: Advances in architectural geometry 2016. 2016, p. 344–63.
[24] Oval R, Nuh M, Costa E, Madyan OA, Orr J, Shepherd P. A prototype low-carbon segmented concrete shell building floor system. Structures 2023;49:124–38.
[25] Chen R, Qiu P, Song P, Deng B, Wang Z, He Y. Masonry Shell Structures with Discrete Equivalence Classes. ACM Trans Graph 2023;42(4).
[26] Loing V, Baverel O, Caron J-F, Mesnil R. Free-form structures from topologically interlocking masonries. Autom Constr 2020;113:103117.
[27] Kao GT-C, Iannuzzo A, Thomaszewski B, Coros S, Van Mele T, Block P. Coupled Rigid-Block Analysis: Stability-Aware Design of Complex Discrete-Element Assemblies. Comput Aided Des 2022;146:103216.
[28] Deuss M, Panozzo D, Whiting E, Liu Y, Block P, Sorkine-Hornung O, et al. Assembling self-supporting structures. ACM Trans Graph 2014;33(6).
[29] Bruun EP, Pastrana R, Paris V, Beghini A, Pizzigoni A, Parascho S, et al. Three cooperative robotic fabrication methods for the scaffold-free construction of a masonry arch. Autom Constr 2021;129:103803.
[30] Wang Z, Kennel-Maushart F, Huang Y, Thomaszewski B, Coros S. A temporal coherent topology optimization approach for assembly planning of bespoke frame structures. ACM Trans Graph 2023;42(4).
[31] Laccone F, Menicagli S, Cignoni P, Malomo L. Static- and fabrication-aware segmented concrete shells made of post-tensioned precast flat tiles. In: Gabriele S, Manuello A, Marmo F, Micheletti A, editors. Shell and spatial structures: proceedings of IWSS 2023. A springer book series lecture notes in civil engineering, 2023, http://dx.doi.org/10.1007/978-3-031-44328-2_1.
[32] Peng C-H, Jiang C, Wonka P, Pottmann H. Checkerboard Patterns with Black Rectangles. ACM Trans Graph 2019;38(6).
[33] Laccone F, Malomo L, Froli M, Cignoni P, Pietroni N. Automatic Design of Cable-Tensioned Glass Shells. Comput Graph Forum 2020;39(1):260–73.
[34] Johnson SG. The NLopt nonlinear-optimization package. 2021, URL: https://github.com/stevengj/nlopt.
[35] Systèmes D. Abaqus analysis user's manual, vol. 40, Providence, RI, USA: Simulia Corp.; 2022.
[36] McNeel R, Associates. Grasshopper generative modeling for Rhino. 2020, http://www.grasshopper3d.com,
[37] Preisinger C, Heimrath M. Karamba - A toolkit for parametric structural design. 24, (2):Taylor & Francis; 2014, p. 217–21,
[38] Rechenraum GmbH. goat® optimization solver component for Rhino's Grasshopper. 2021, Computer software documentation, http://www.rechenraum.com/.